

NAVIGATION AND DISPERSION ANALYSIS OF THE FIRST ORION EXPLORATION MISSION

Christopher D'Souza* and Renato Zanetti†

This paper presents the Orion EM-1 Linear Covariance Analysis for the DRO mission. The $|\Delta\mathbf{V}|$ statistics for each maneuver are presented. In particular, the statistics of the lunar encounters and the Entry Interface are presented.

INTRODUCTION

This paper seeks to present the navigation and dispersion analysis for the Orion EM-1 Distant Retrograde Orbit (DRO) mission. It is based upon the theory presented in Maybeck.¹ This is a further analysis of the DRO trajectory along the lines of what was presented by D'Souza and Zanetti.²

The accuracy of the flight-path angle at Entry Interface* (EI) is driven by several factors including the navigation, targeting, and burn execution errors at the time of the last mid-course maneuver, and unaccounted trajectory perturbations between the last mid-course maneuver and EI. Apollo missions tolerated a maximum flight path angle error at EI of ± 1 degree, with half of this error allocated to navigation. A similar criterion is employed in this study.

Perturbations are a major source of errors in the cislunar navigation performance of Orion. In a perfect world all the sources of perturbations would be modeled in the filter dynamics. However, computational limitations (and fundamental knowledge) preclude such extensive modeling. Therefore, the primary sources of perturbations are characterized. In particular there are three categories of unmodeled acceleration: propulsive sources, gravitational perturbations, and solar radiation pressure. Only propulsive errors are included in this analysis; the gravitational and solar radiation pressure are not included; they will be included in a future study. For EM1, the gravitational and solar radiation pressure errors are several orders of magnitude below the thrusting sources. The propulsive sources considered are: attitude deadbands, attitude slews, CO₂ venting, and sublimator venting.

Linear covariance techniques are used to perform the analysis for the Orion Cislunar missions. This comports well for the navigation system design since the cislunar navigation system on Orion will be an Extended Kalman Filter. Many of the same states and dynamics used in the linear covariance analysis will be used in the on-board cislunar navigation system. A preliminary design of the cislunar navigation system is presented. This is supported by linear covariance analyses which provides navigation performance, trajectory dispersion performance and $|\Delta\mathbf{V}|$ usage.

The paper is organized as follows: Section 2 will contain a brief description of linear covariance analysis. In Section 3, the navigation system will be described, both the filter dynamics as well as the measurement. Section 4 will contain results of this analysis. Finally, a few concluding comments are made in Section 5.

*Aerospace Engineer, EG6, NASA/JSC, Houston, TX.

†Aerospace Engineer, EG6, NASA/JSC, Houston, TX.

*For Orion Entry Interface is normally taken to be at an altitude of 400,000 ft.

LINEAR COVARIANCE ANALYSIS

This investigation is performed using linear covariance (LinCov) analysis techniques.^{2,3} The state vector is

$$\mathbf{x} = \left\{ \mathbf{r}^T \quad \mathbf{v}^T \quad \boldsymbol{\theta}^T \quad \mathbf{m}_{op}^T \quad \mathbf{m}_{tr}^T \quad \mathbf{b}_{cent}^T \quad b_{pd} \right\}^T. \quad (1)$$

where \mathbf{r} is the inertial position of the vehicle with respect to the primary body, \mathbf{v} is the corresponding inertial velocity with respect to the primary, $\boldsymbol{\theta}$ is the attitude error, \mathbf{m}_{op} is the misalignment of the optical instrument, \mathbf{m}_{tr} is the bias position of the instrument with respect to the navigation base, \mathbf{b}_{cent} is the bias of the planetary centroid measurement, and b_{pd} is the bias of the planetary diameter measurement.

The nominal trajectory is obtained by integrating the nominal dynamics model with an Encke-Nystrom method.² Neither the attitude error $\delta\boldsymbol{\theta}$ nor its uncertainty are integrated in this analysis. The nominal attitude is known at any time and it does not need to be calculated. The attitude estimation error covariance is constant and is driven by the star tracker accuracy. The attitude navigation dispersion covariance is constant and is given by the attitude control dead-band. Before the star elevation is determined, the vehicle slews in preparation for measurement acquisition. This attitude maneuver is performed by the onboard thrusters and is assumed to be instantaneous. Due to thruster misalignment, this maneuver adds uncertainty to the translational states. After the batch of measurements is available, the vehicle returns to its nominal attitude. In linear covariance analysis, the difference between the true state and the nominal state is defined as the environment dispersion

$$\delta\mathbf{x} \triangleq \mathbf{x} - \bar{\mathbf{x}}. \quad (2)$$

The difference between the estimated state and the nominal state is defined as the navigation dispersion

$$\delta\hat{\mathbf{x}} \triangleq \hat{\mathbf{x}} - \bar{\mathbf{x}}. \quad (3)$$

Finally, the difference between the true state and the estimated state, is defined as the estimation error, sometimes referred to as the onboard navigation error

$$\mathbf{e} \triangleq \mathbf{x} - \hat{\mathbf{x}}. \quad (4)$$

Following the standard Kalman filter assumptions, the difference between the nominal and estimated models is represented with zero-mean, white noise. The estimated state evolves as

$$\dot{\hat{\mathbf{x}}} = \mathbf{f}(\hat{\mathbf{x}}), \quad (5)$$

where \mathbf{f} is a nonlinear function representing the system dynamics as modeled by the filter. The evolution of the nominal state is modeled as

$$\dot{\bar{\mathbf{x}}} = \bar{\mathbf{f}}(\bar{\mathbf{x}}) = \mathbf{f}(\bar{\mathbf{x}}) + \mathbf{v}, \quad (6)$$

where $\bar{\mathbf{f}}$ is a nonlinear function representing the state dynamics as modeled in designing the nominal trajectory. The nominal dynamics $\bar{\mathbf{f}}$ may be higher fidelity than the filter's dynamics \mathbf{f} . The vector \mathbf{v} represents the dynamics modeled in the nominal trajectory but neglected in the filter models. In Kalman filtering, the difference between the true dynamics and the filter's dynamics is called process noise. While these unmodeled dynamics are not actually white noise, they are modeled as such. The power spectral density of process noise is then tuned to achieve good performance. The same procedure is used here. In order to capture the difference between the two dynamical models, \mathbf{v} is modeled as a zero-mean white noise process with power spectral density $\hat{\mathbf{Q}}$. The goal is to represent the increased value of the navigation dispersion during propagation due to the difference between the nominal and filter's dynamical models.

The evolution of the navigation dispersion can be approximated to first-order as

$$\delta\dot{\hat{\mathbf{x}}} = \dot{\hat{\mathbf{x}}} - \dot{\bar{\mathbf{x}}} = \mathbf{f}(\bar{\mathbf{x}} + \delta\hat{\mathbf{x}}) - \mathbf{f}(\bar{\mathbf{x}}) - \mathbf{v} \simeq \mathbf{F}(\bar{\mathbf{x}})\delta\hat{\mathbf{x}} - \mathbf{v}. \quad (7)$$

The evolution of the navigation dispersion covariance is governed by

$$\dot{\hat{\mathbf{P}}} = \mathbf{F}(\bar{\mathbf{x}})\hat{\mathbf{P}} + \hat{\mathbf{P}}\mathbf{F}(\bar{\mathbf{x}})^T + \hat{\mathbf{Q}}. \quad (8)$$

Similarly, the true state is modeled to evolve as

$$\dot{\mathbf{x}} = \mathbf{f}(\mathbf{x}) + \boldsymbol{\nu}. \quad (9)$$

The evolution of the estimation error is given by

$$\dot{\mathbf{e}} = \dot{\mathbf{x}} - \dot{\hat{\mathbf{x}}} \simeq \mathbf{f}(\bar{\mathbf{x}}) + \mathbf{F}(\bar{\mathbf{x}})(\mathbf{x} - \bar{\mathbf{x}}) + \boldsymbol{\nu} - \mathbf{f}(\bar{\mathbf{x}}) - \mathbf{F}(\bar{\mathbf{x}})(\hat{\mathbf{x}} - \bar{\mathbf{x}}) = \mathbf{F}(\bar{\mathbf{x}})\mathbf{e} + \boldsymbol{\nu}. \quad (10)$$

Vector $\boldsymbol{\nu}$ is modeled as zero mean white noise with power spectral density \mathbf{Q} . The onboard covariance \mathbf{P} evolves as

$$\dot{\mathbf{P}} = \mathbf{F}(\bar{\mathbf{x}})\mathbf{P} + \mathbf{P}\mathbf{F}(\bar{\mathbf{x}}) + \mathbf{Q}. \quad (11)$$

Notice that the Jacobian \mathbf{F} could be evaluated at the estimated state $\hat{\mathbf{x}}$ instead of the nominal state $\bar{\mathbf{x}}$, as in the extended Kalman filter.

Finally

$$\delta\dot{\mathbf{x}} = \dot{\mathbf{x}} - \dot{\hat{\mathbf{x}}} \simeq \mathbf{F}(\bar{\mathbf{x}})\delta\mathbf{x} + \boldsymbol{\nu} - \boldsymbol{v} \quad (12)$$

and $\bar{\mathbf{P}}$ evolves as

$$\dot{\bar{\mathbf{P}}} = \mathbf{F}(\bar{\mathbf{x}})\bar{\mathbf{P}} + \bar{\mathbf{P}}\mathbf{F}(\bar{\mathbf{x}}) + \bar{\mathbf{Q}}. \quad (13)$$

Notice that $\bar{\mathbf{Q}} = \mathbf{Q} + \hat{\mathbf{Q}}$ if $\boldsymbol{\nu}$ and \boldsymbol{v} are assumed to be uncorrelated.

THE ORION CISLUNAR NAVIGATION FILTER

The Orion onboard navigation filter will be required to estimate the position and velocity of the spacecraft. A decision has been made to separate out the attitude determination filter. It is important, however, to maintain an estimate of the attitude error of the vehicle since the measurements being taken are inherently angle measurements. Hence, navigation state vector is comprised of the following

$$\mathbf{x} = \left\{ \mathbf{r}^T \quad \mathbf{v}^T \quad \boldsymbol{\theta}^T \quad \mathbf{m}_{op}^T \quad \mathbf{m}_{tr}^T \quad \mathbf{b}_{cent}^T \quad b_{pd} \right\}^T. \quad (14)$$

where \mathbf{r} is the inertial position of the vehicle with respect to the primary body, \mathbf{v} is the corresponding inertial velocity with respect to the primary, $\boldsymbol{\theta}$ is the attitude error, \mathbf{m}_{op} is the misalignment of the optical instrument, \mathbf{m}_{tr} is the bias position of the instrument with respect to the navigation base, \mathbf{b}_{cent} is the bias of the planetary centroid measurement, and b_{pd} is the bias of the planetary diameter measurement.

The Filter Dynamics

Since this filter operates once Orion is away from Earth (and outside of GPS range), the primary forces governing the motion of the vehicle are the gravitational forces of the Earth, the Moon, and the Sun. The trajectory is designed taking into account all three of these bodies. Whereas the equations of motion are formulated with respect to a central body, this (central body) changes depending on which sphere of influence the vehicle is subject to.

The equations of motion for the Earth-Sun-Moon system are

$$\ddot{\mathbf{r}}_{PV} = -\frac{\mu_P}{r_{PV}^3}\mathbf{r}_{PV} - \mu_Q \left[\frac{\mathbf{r}_{QV}}{r_{QV}^3} + \frac{\mathbf{r}_{PQ}}{r_{PQ}^3} \right] - \mu_S \left[\frac{\mathbf{r}_{SV}}{r_{SV}^3} + \frac{\mathbf{r}_{PS}}{r_{PS}^3} \right] \quad (15)$$

where \mathbf{r}_{PV} is the position of the vehicle (V) with respect to the primary body (P), \mathbf{r}_{QV} is the position of the vehicle with respect to the secondary body (Q), \mathbf{r}_{PQ} is the position of the secondary body with respect to the primary body, \mathbf{r}_{SV} is the position of the vehicle with respect to the Sun (S), and \mathbf{r}_{PS} is the position of the Sun with respect to the primary body. The geometry is shown in Figure 2. In many applications, these equations are integrated by a Runge-Kutta or Runge-Kutta-Fehlberg fixed-step or variable-step algorithms.

However, blindly applying a standard fourth-order Runge-Kutta method can lead to numerical errors (if large step sizes are taken) not to mention inefficiencies (if small step sizes are taken). The Encke-Nyström method has been shown to have none of these deficiencies – large step sizes can be taken and numerical precision maintained at the same time.

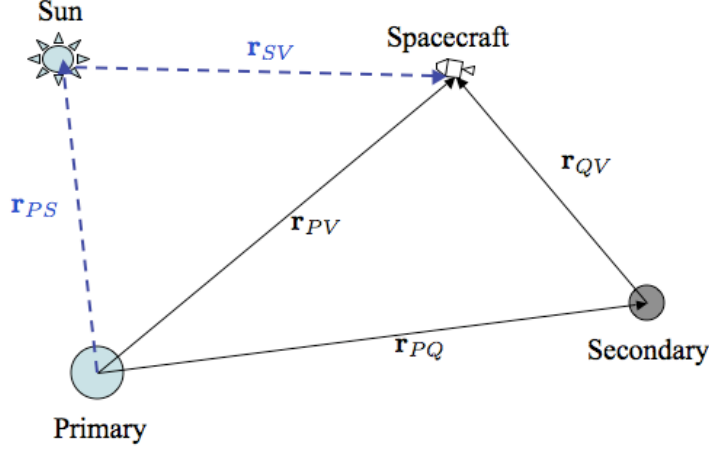


Figure 1. The Earth-Sun-Moon-Vehicle Geometry

The Encke-Nyström Method The Encke-Nyström method has an illustrious legacy. Unlike the Cowell's method, only the perturbations away from two-body motion are integrated. As such, the perturbations being integrated are small and excellent numerical precision is retained. In addition, since the force-field under which the equations of motion being integrated is conservative, and since the velocity derivatives are expressed in terms of the position only, a Nyström formulation of integration is used. The disadvantage of this method is that there is a bit of mathematical set-up required. However, if one is willing to pay this price, the dividends are enormous – both in terms of precision and computation time. The equations which are integrated are as follows:

$$\ddot{\mathbf{r}}_{PV} = -\frac{\mu_P}{r_{PV}^3} \mathbf{r}_{PV} - \frac{\mu_Q}{r_{QV}^3} [f(q_Q) \mathbf{r}_{PQ} + \mathbf{r}_{PV}] - \frac{\mu_S}{r_{SV}^3} [f(q_S) \mathbf{r}_{PS} + \mathbf{r}_{PV}] \quad (16)$$

where

$$q_{()} = \frac{(\mathbf{r}_{PV} - 2\mathbf{r}_{P(())}) \cdot \mathbf{r}_{PV}}{r_{P(())}^2}$$

$$f(q_{()}) = q_{()} \frac{3 + 3q_{()} + q_{()}^2}{1 + (1 + q_{()})^{3/2}}$$

This formulation was used in the Apollo program.[?] It should be noted that Eqs.(15) and (16) are mathematically equivalent.

The Measurements

The measurements are the planetary centroid and planetary apparent diameter as seen by the optical camera. We are interested in the coordinates in the image plane, (u, v) , such that the vector to the point of interest is

$$\mathbf{u} = \begin{bmatrix} \frac{u_p - u}{f_{sx}} \\ \frac{v_p - v}{f_{sy}} \\ 1 \end{bmatrix} \quad (17)$$

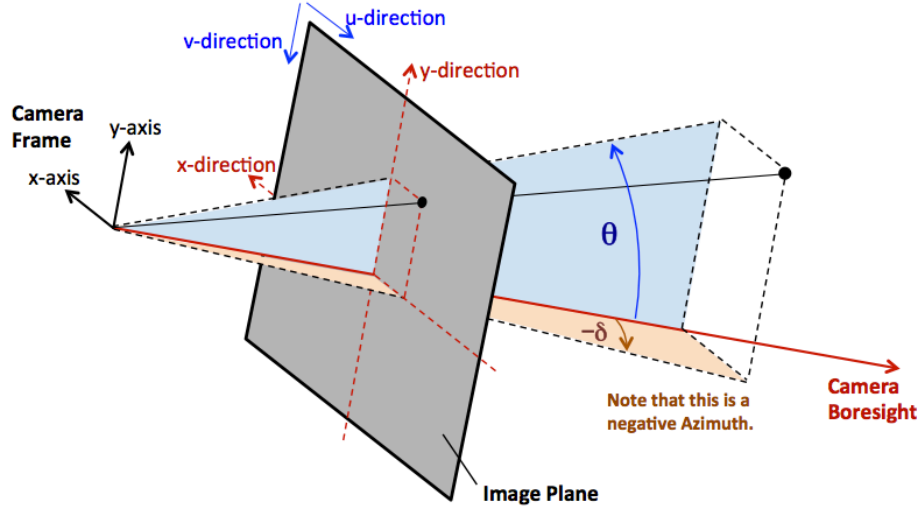


Figure 2. Camera Image Plane Coordinates

where, as seen in Figure 2, (u_p, v_p) are the coordinates of the principal point (i.e. the point where the camera boresight intersects the image plane), s_x and s_y are the x -axis and y -axis scale factors, respectively, in units of pixels/length, and f is the focal length of the camera optics.

The line-of-sight unit vector can also be expressed in terms of the horizontal and vertical angles, δ and θ , where

$$\tan \delta = \frac{u_p - u}{f s_x}; \quad \tan \theta = \frac{v_p - v}{f s_y} \quad (18)$$

so that the unit vector is

$$\mathbf{i}_{P/cam}^{cam} = \frac{1}{\sqrt{\tan^2 \delta + \tan^2 \theta + 1}} \begin{bmatrix} \tan \delta \\ \tan \theta \\ 1 \end{bmatrix} \quad (19)$$

Whereas the geometry of the horizontal and vertical angles in the focal (and image) plane are useful (particularly for correcting for radial distortion), we can directly relate the u, v coordinates to the position of the planet in the camera frame as

$$\frac{u_p - u}{s_x f} = \frac{x_{P/cam}^{cam}}{z_{P/cam}^{cam}}; \quad \frac{v_p - v}{s_y f} = \frac{y_{P/cam}^{cam}}{z_{P/cam}^{cam}} \quad (20)$$

where $x_{P/cam}^{cam}$, $y_{P/cam}^{cam}$ and $z_{P/cam}^{cam}$ are the Cartesian coordinates of the planet with respect to the camera expressed in camera coordinates (corresponding to $\mathbf{r}_{P/cam}^{cam}$.)

The optical navigation passes are chosen so as to conclude 1 hour before each maneuver. The measurements, during an optical navigation pass, occur every 30 seconds. This is to allow for the final targeting of the maneuver as well as time to perform an attitude maneuver to get to the maneuver attitude. During those epochs when the maneuvers occurred more than 24 hours apart, navigation passes are scheduled so as to ensure that the onboard state remained reasonable.

Error	Value
U (Radial) Position	30984.0 ft
V Position	196002.0 ft
W (Out-of-Plane) Position	10981.8 ft
U (Radial) Velocity	170.820 ft/s
V Velocity	29.250 ft/s
W (Out-of-Plane) Velocity	42.510 ft/s

Table 1. Translunar Injection Accuracy (3σ)

Type	Value
Quiescent	$3.801 \times 10^{-8} \text{ ft}^2/\text{s}^3$
Active (CM/SM)	$1.410 \times 10^{-4} \text{ ft}^2/\text{s}^3$
Active (CM only)	$8.479 \times 10^{-4} \text{ ft}^2/\text{s}^3$

Table 2. Vehicle Translation Process Noise Characteristics

System Model Parameters

Table 1 contains the data for the injection covariance matrix used in this analysis. Table 2 contains the model for the process noise used during the mission, both quiescent and active. Table 3 contains the maneuver execution errors for this case. Tables 4 and 5 contain the optical navigation camera parameters and error model, respectively.

Maneuver Execution Error	3σ Value
Noise (ft/s)	0.027
Bias (ft/s)	0.009
Scale Factor (ppm)	450.0
Misalignment (deg)	0.03

Table 3. The Maneuver Execution Error Model

Parameter	Value
Field of View	20.0 degrees
Pixel Pitch	2.2 microns
Focal Length	16.0 mm
Focal Plane Array Size	2592 x 1944

Table 4. Optical Camera Characteristics

Error Type	Value
Centroid Measurement Noise	0.14 (1σ) pixels
Diameter Measurement Noise	0.14 (1σ) pixels
Centroid Measurement Markov Steady State	0.07 (1σ) pixels
Diameter Measurement Markov Steady State	0.07 (1σ) pixels
Misalignment Markov Steady State	15.0 (1σ) arc-seconds
Centroid Measurement Markov Time Constant	4.0 hrs
Diameter Measurement Markov Time Constant	4.0 hrs
Misalignment Markov Time Constant	60.0 sec

Table 5. Optical Camera Error Model

Concept of Operations of Maneuvers

It was assumed that there were 4 outbound trajectory correction (OTC) maneuvers on the leg from the Earth to the Moon, a single Outbound Powered Flyby (OPF) maneuver targeted for the DRO insertion point, two outbound correction maneuvers between the PFM-1 and the DRO Insertion (DRO-I) point. Once on the DRO, there were 3 (DRO) Orbit Maneuvers (OM) spaced approximately equally, all targeting the DRO Departure maneuver point. After the DRO Departure (DRO-D) Maneuver, there are two correction maneuvers targeted the perilune conditions of the Return Powered Flyby (RPF) maneuver. Finally, at after RPF, there are three correction maneuvers (RTC 4-6). These maneuvers and their TIGs are outlined in Table 6.

Maneuver #	Type	t_{ig} (hrs)	$ \Delta V_{nom} $ (ft/s)
1	OTC-1	6.81	0.000
2	OTC-2	25.81	0.000
3	OTC-3	81.60	0.000
4	OTC-4	97.60	0.000
5	OPF	103.60	572.627
6	OTC-5	122.41	0.000
7	OTC-6	144.00	0.000
8	DRI	169.21	797.479
9	OM-1	204.00	0.000
10	OM-2	240.00	0.000
11	OM-3	276.00	0.000
12	DRD	316.80	278.567
13	RTC-1	372.01	0.000
14	RTC-2	426.01	0.000
15	RTC-3	477.62	0.000
16	RPF	483.62	827.866
17	RTC-4	501.61	0.000
18	RTC-5	591.04	0.000
19	RTC-6	607.04	0.000
Total			2476.539

Table 6. The Maneuver Plan

THE NAVIGATION ERRORS AND TRAJECTORY DISPERSIONS

The EM-1 Mission is divided into five phases: the Earth-Moon (TransLunar) Phase, the Moon-to-DRO phase, the DRO-orbit phase, the DRO-to-Moon phase and the Moon-to-Earth (transEarth) phase. Whereas the navigation errors and trajectory dispersions are important in each phase, of particular importance are the Earth-to-Moon, DRO-to-Moon and the Moon-to-Earth phases. Of ultimate importance is the Moon-to-Earth Phase because that determines whether the crew can return safely to Earth. Of course, the epoch of concern in this phase is the Entry Interface (EI) condition. In what follows the trajectory dispersions and navigation errors in each of these three phases will be detailed.

The Outbound Lunar Flyby with Optical Navigation

The navigation errors and trajectory dispersions for the EM-1 mission with optical navig mapped to the B-plane are presented in Figures 3-4. For a sense of scale, these navigation errors and trajectory dispersions mapped to the B-plane with the (radius of the) Moon plotted for scale are presented in Figures 5-6. The trajectory dispersions at the time of the OPF maneuver are presented in Table 7. The B-plane trajectory dispersions at the time of the OPF maneuver are presented in Table 8.

The Return Lunar Flyby with Optical Navigation

The navigation errors and trajectory dispersions mapped to the B-plane are presented in Figures 7-8. For a sense of scale, these navigation errors and trajectory dispersions mapped to the B-plane with the (radius of the) Moon plotted for scale are presented in Figures 9-10. The trajectory dispersions at the time of the RPF maneuver are presented in Table 9. The B-plane trajectory dispersions at the time of the RPF maneuver are presented in Table 10.

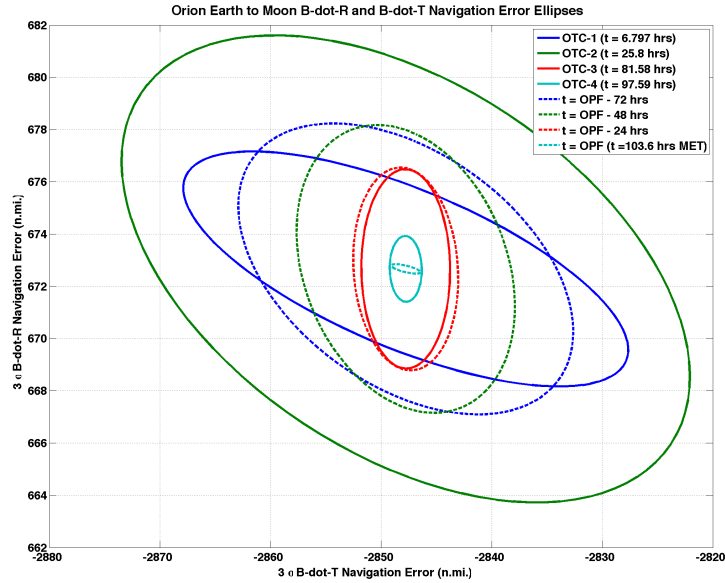


Figure 3. The Translunar Navigation Errors mapped to the B-plane

Type	OPF 3σ Value
Periapsis Altitude	0.7910 n.m.
Inclination	0.0212 deg
Argument of Periapsis	0.0707 deg
C_3	41117.2186 ft ² /s ²

Table 7. The Trans-Lunar Delivery 3σ Statistics at OPF

Type	OPF 3σ Value
B·T	7.6472 n.m.
B·R	1.7305 n.m.
Linearized Time-of-Flight	0.7220 sec

Table 8. The Trans-Lunar Delivery 3σ B-plane Statistics at OPF

The Trans-Earth Phase

The navigation errors mapped to Entry Interface errors are presented in Figures 11-14. The trajectory disperions mapped to Entry Interface trajectory disperions are presented in Figures 15-18.

Summary of the DRO Mission with Optical Navigation

Table 11 contains the $|\Delta\mathbf{V}|$ statistics for this Maneuver Profile. The quantity $|\Delta\mathbf{V}|_{99.73}$ represents the $|\Delta\mathbf{V}|$ values, 99.73% of samples of which are below this value (for a univariate Gaussian distribution $\Pr(\mu - 3\sigma \leq x \leq \mu + 3\sigma) \approx .9973$). In order to determine this, the covariance was sampled 10,000 times and from this the $|\Delta\mathbf{V}|_{99.73}$ and the other statistics (μ and σ of the $|\Delta\mathbf{V}|$) were computed.⁴

Table 12 contains the delivery statistics at the EI point.

CONCLUSIONS AND RECOMMENDATIONS

This paper has detailed the linear covariance analysis for the EM-1 DRO mission. The major contributor to the $|\Delta\mathbf{V}|$ usage is the TLI error; hence if the accuracy of TLI can be improved (to even meeting the requirements) there would be a substantial propellant savings. In addition, if the epoch of the first correction

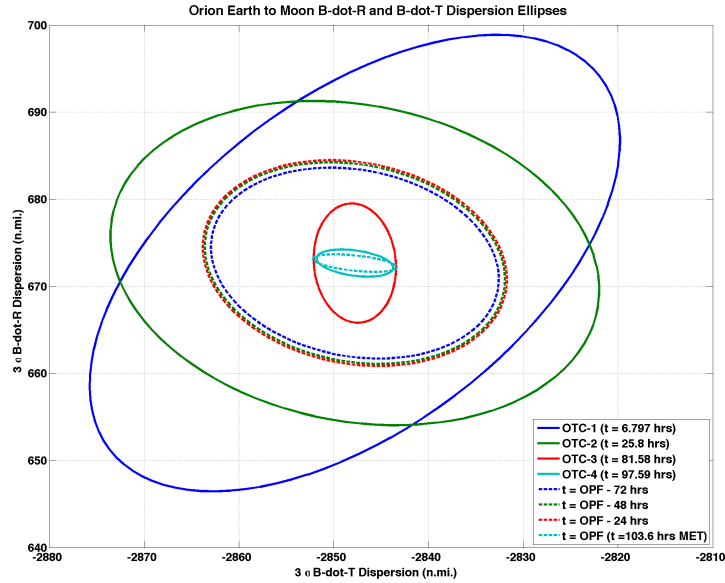


Figure 4. The Translunar Trajectory Dispersion mapped to the B-plane

Type	RPF 3σ Value
Periapsis Altitude	0.5576 n.m.
Inclination	0.0301 deg
Argument of Periapsis	1.9839 deg
C_3	124451.4910 ft ² /s ²

Table 9. The DRO-to-Moon Delivery 3σ Statistics at RPF

Type	RPF 3σ Value
B-T	11.9024 n.m.
B-R	4.7242 n.m.
Linearized Time-of-Flight	0.5284 sec

Table 10. The DRO-to-Moon Delivery 3σ B-plane Statistics at RPF

maneuver (OTC-1) were to occur at TLI + 3 hours, that would result in a substantial propellant savings. Finally, if the length of the optical navigation passes for the final two maneuvers (RTC-5 and RTC-6) were to be increased to 2 hours (from 1 hour), that would improve the trajectory dispersions at EI.

Acknowledgements

Many thanks to Sara Scarritt for generating the lincov measurement partials and to Greg Holt and Dave Woffinden for many helpful discussions.

REFERENCES

- [1] P. Maybeck, *Stochastic Models, Estimation and Control, Vol. 1*. New York, NY: Academic Press, 1979.
- [2] C. D'Souza and R. Zanetti, "Navigation Design and Analysis for the Orion Earth-Moon Mission," *AAS/AIAA Space Flight Mechanics Conference*, February 2014.
- [3] D. K. Geller, "Linear Covariance Techniques for Orbital Rendezvous Analysis and Autonomous Onboard Mission Planning," *Journal of Guidance, Navigation and Dynamics*, Vol. 29, No. 6, 2006, pp. 1404–1414.
- [4] W. Bollman and C. Chadwick, "Statistics of ΔV Magnitude for a Trajectory Correction Maneuver Containing Deterministic and Random Components," *Proceedings of the AIAA/AAS Astrodynamics Conference*, August 1982.

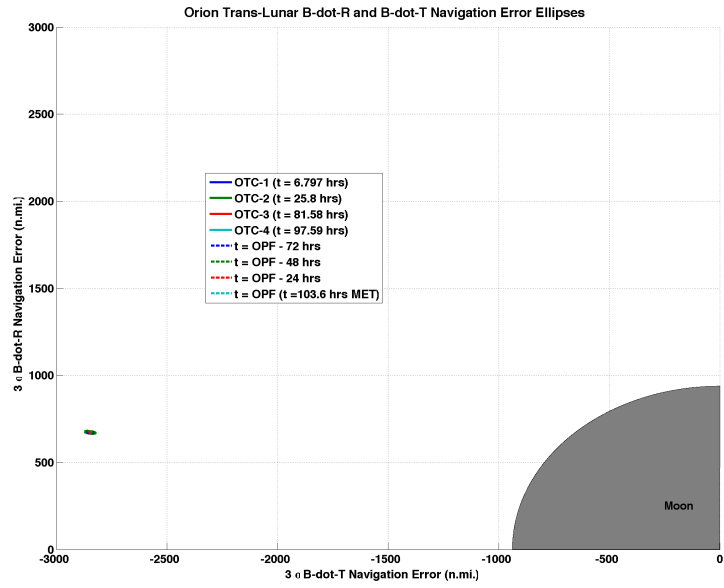


Figure 5. The Translunar Navigation Errors mapped to the B-plane (with Moon for scale)

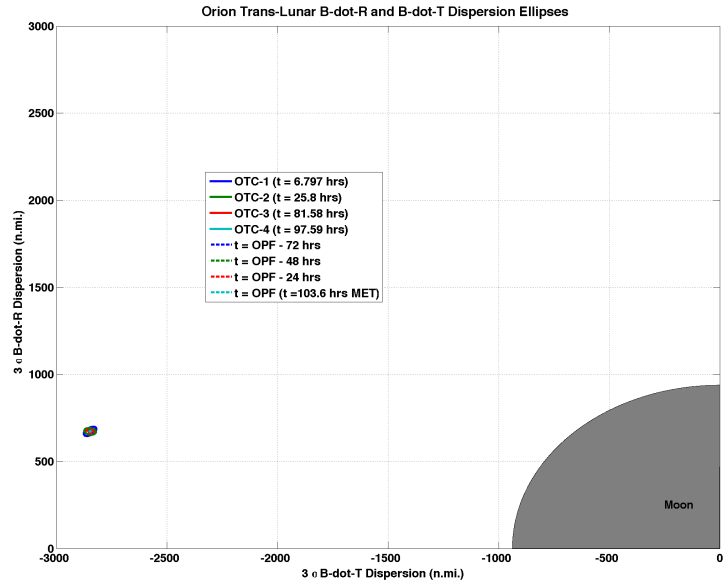


Figure 6. The Translunar Trajectory Dispersion mapped to the B-plane (with Moon for scale)

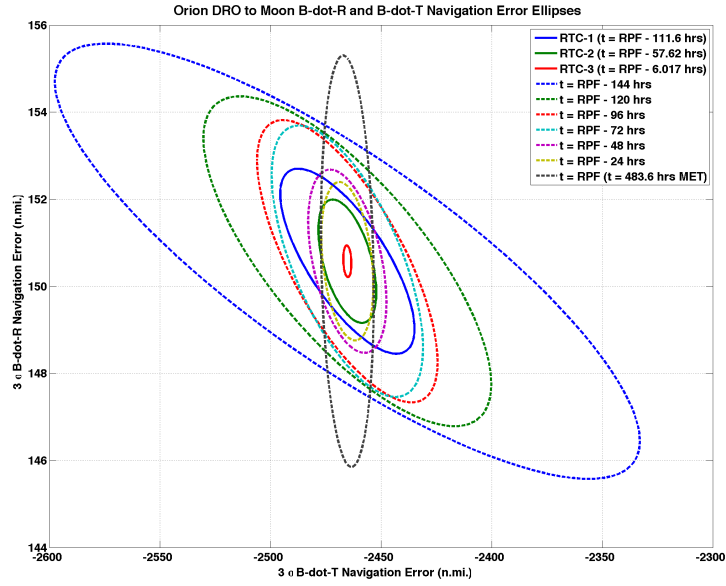


Figure 7. DRO-to-Moon Navigation Errors mapped to the B-plane

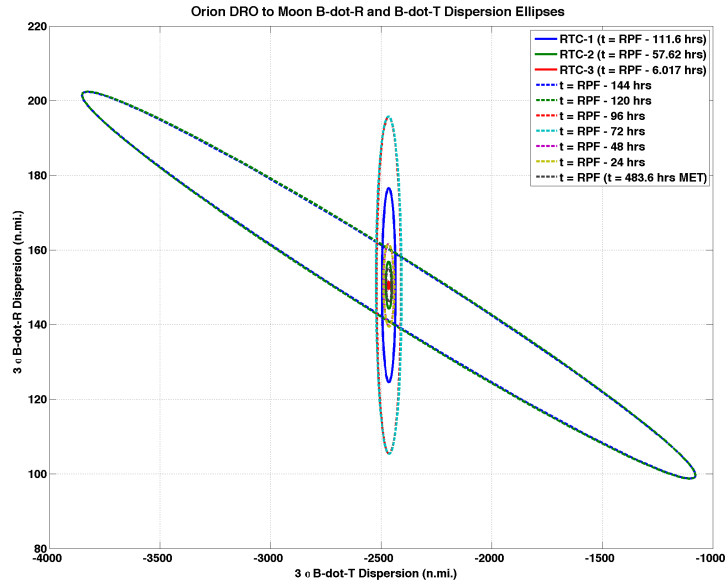


Figure 8. DRO-to-Moon Trajectory Dispersion mapped to the B-plane

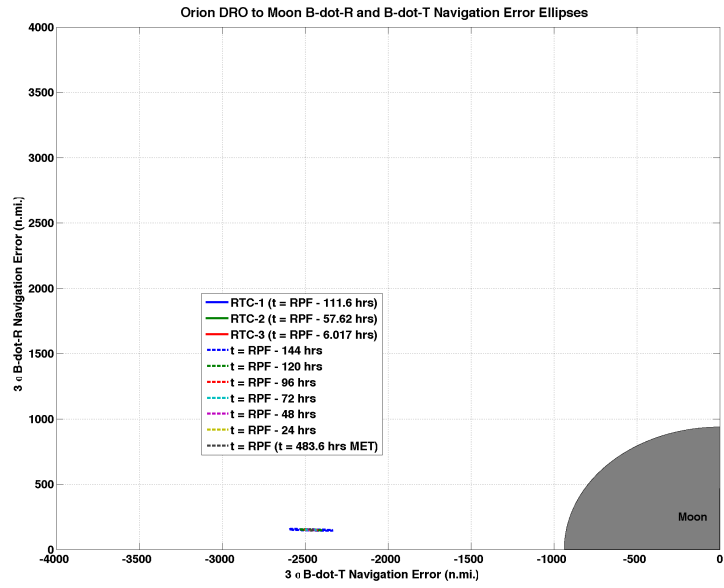


Figure 9. DRO-to-Moon Navigation Errors mapped to the B-plane (with Moon for scale)

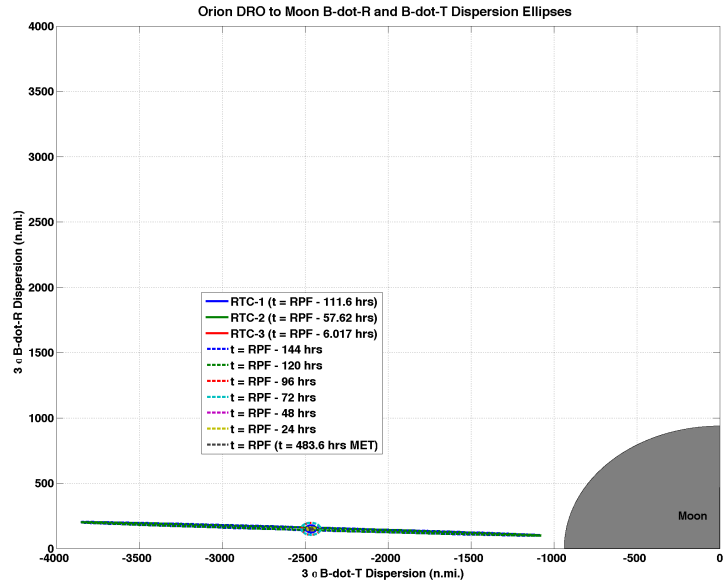


Figure 10. DRO-to-Moon Trajectory Dispersion mapped to the B-plane (with Moon for scale)

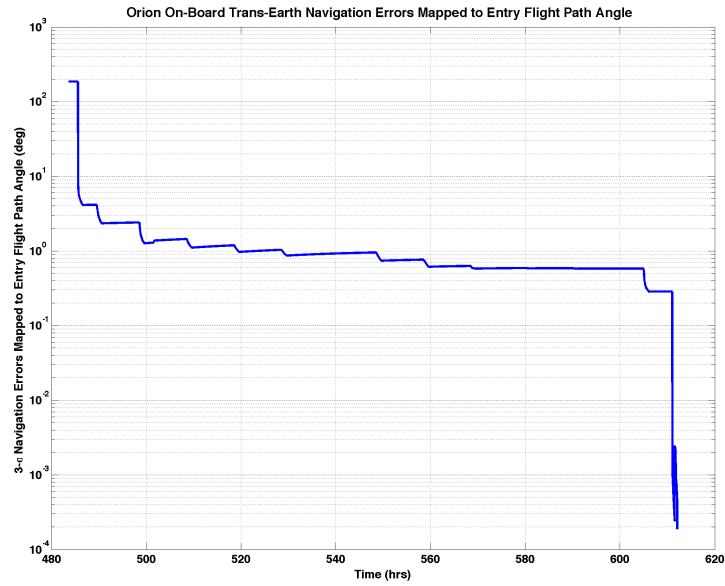


Figure 11. The Onboard Navigation Errors Mapped to Entry Interface Flight Path Angle Errors

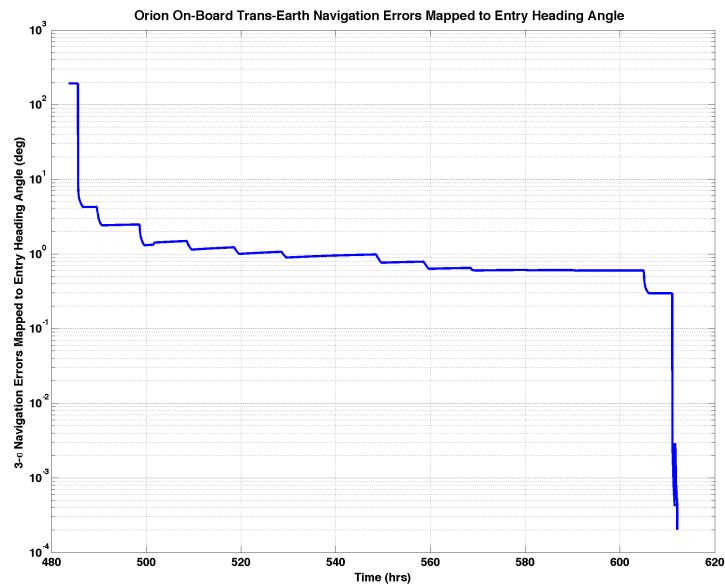


Figure 12. The Onboard Navigation Errors Mapped to Entry Interface Heading Angle Errors

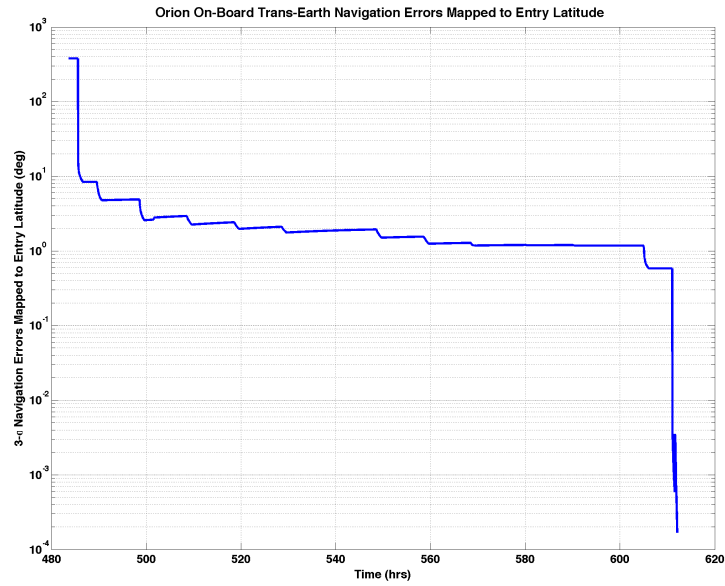


Figure 13. The Onboard Navigation Errors Mapped to Entry Interface Latitude Errors

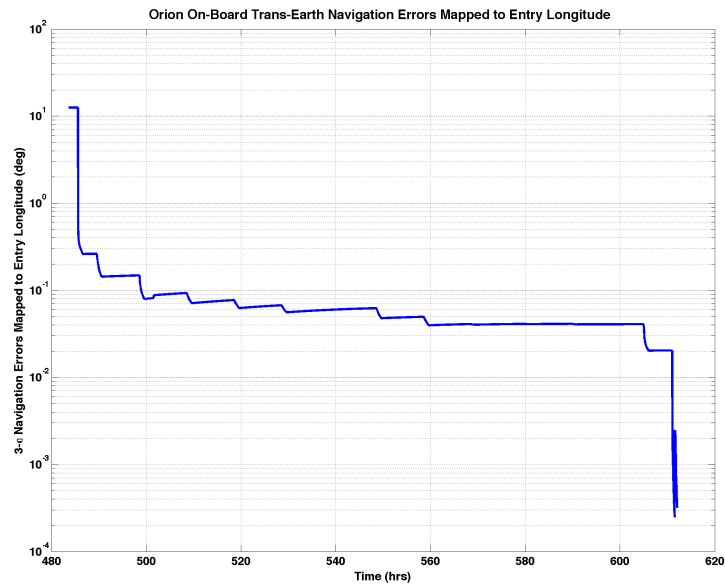


Figure 14. The Onboard Navigation Errors Mapped to Entry Interface Longitude Errors

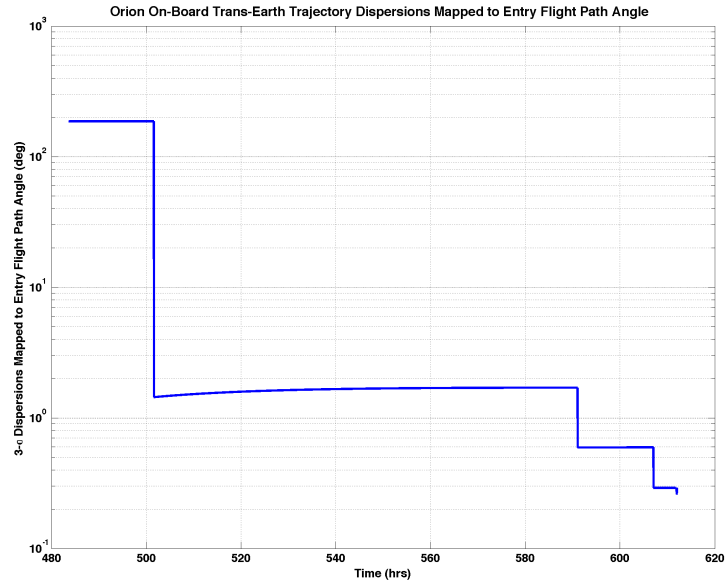


Figure 15. The Trans-Earth Trajectory Dispersions Mapped to Entry Interface Flight Path Angle Dispersions

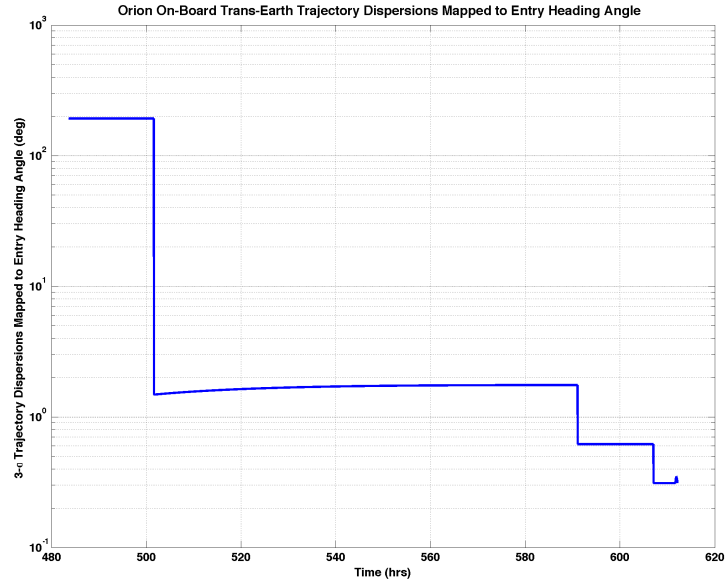


Figure 16. The Trans-Earth Trajectory Dispersions Mapped to Entry Interface Heading Angle Dispersions

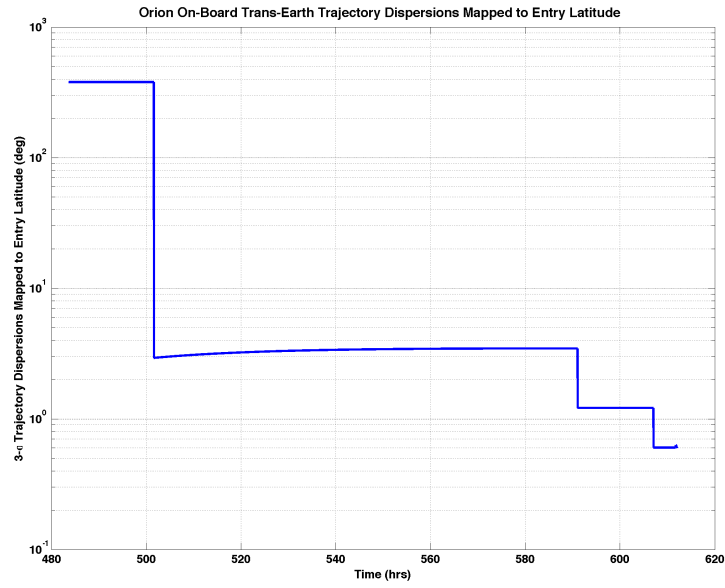


Figure 17. The Trans-Earth Trajectory Dispersions Mapped to Entry Interface Latitude Dispersions

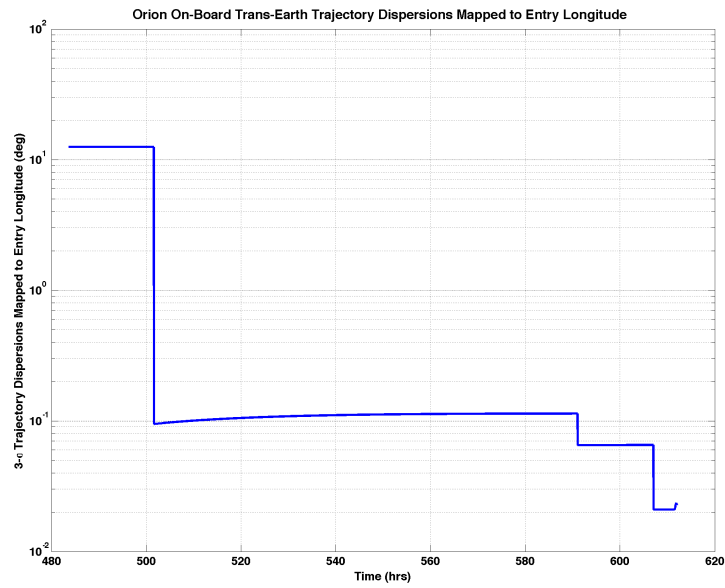


Figure 18. The Trans-Earth Trajectory Dispersions Mapped to Entry Interface Longitude Dispersions

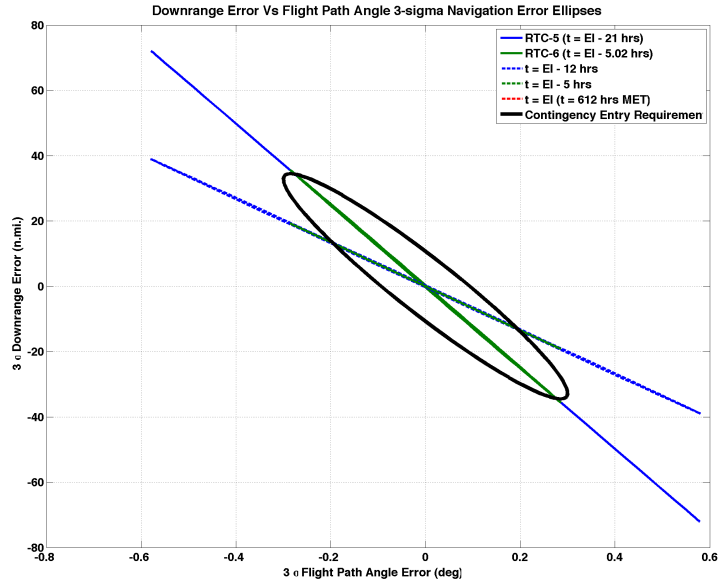


Figure 19. The Trans-Earth Entry Interface Conditions Mapped Downrange vs Flight Path Angle Navigation Error Ellipses

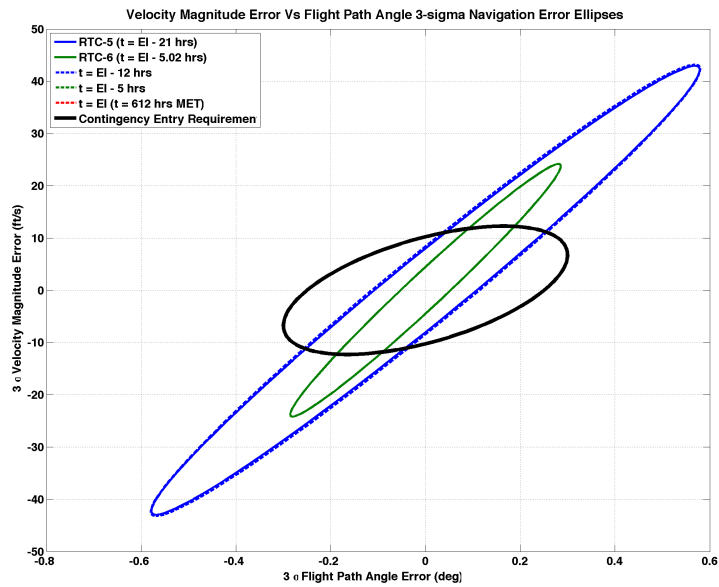


Figure 20. The Trans-Earth Entry Interface Conditions Mapped Velocity Magnitude vs Flight Path Angle Navigation Error Ellipses

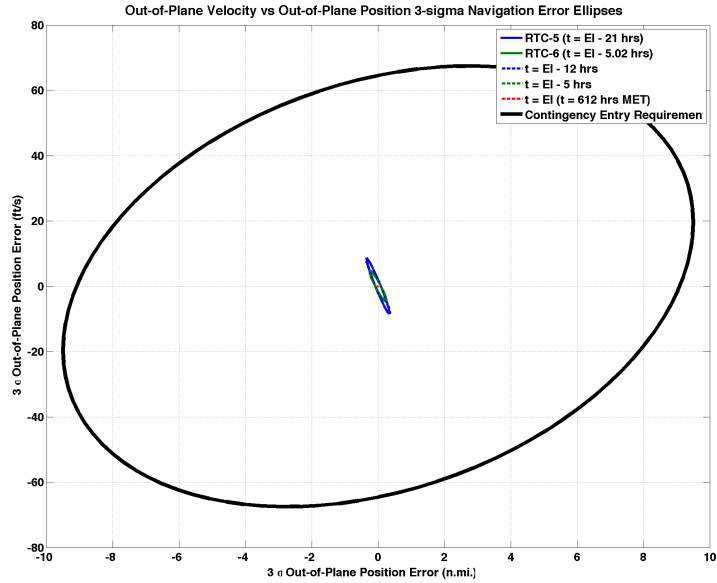


Figure 21. The Trans-Earth Entry Interface Conditions Mapped Crossrange Position vs Crossrange Velocity Navigation Error Ellipses

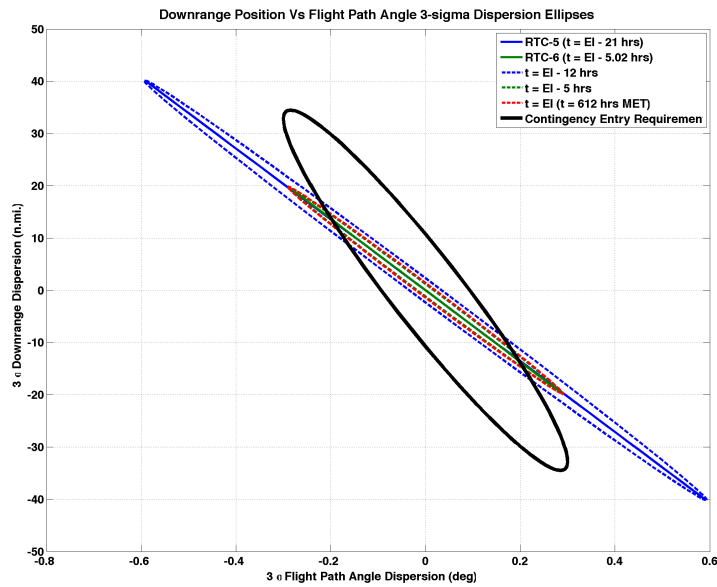


Figure 22. The Trans-Earth Entry Interface Conditions Mapped Downrange vs Flight Path Angle Trajectory Dispersion Ellipses

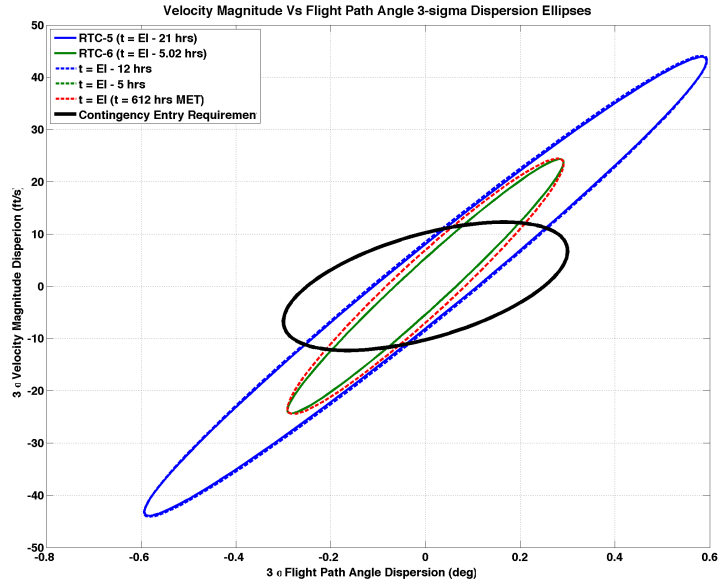


Figure 23. The Trans-Earth Entry Interface Conditions Mapped Velocity Magnitude vs Flight Path Angle Trajectory Dispersion Ellipses

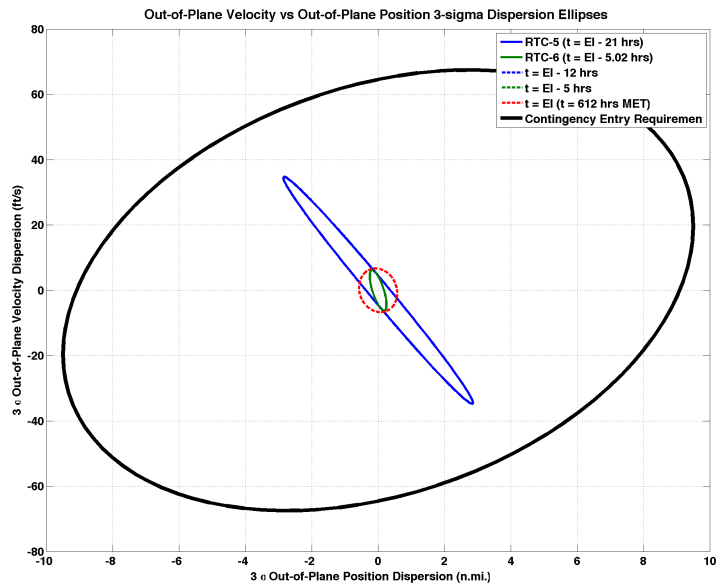


Figure 24. The Trans-Earth Entry Interface Conditions Mapped Crossrange Position vs Crossrange Velocity Trajectory Dispersion Ellipses

Maneuver #	Type	t_{ig} (hrs)	$ \Delta\mathbf{V} _{99.73}$ (ft/s)
1	OTC-1	6.81	46.666
2	OTC-2	25.81	0.360
3	OTC-3	81.60	2.111
4	OTC-4	97.60	3.210
5	OPF	103.60	578.689
6	OTC-5	122.41	33.569
7	OTC-6	144.00	11.349
8	DRI	169.21	798.070
9	OM-1	204.00	47.118
10	OM-2	240.00	23.124
11	OM-3	276.00	1.675
12	DRD	316.80	279.236
13	RTC-1	372.01	16.363
14	RTC-2	426.01	3.341
15	RTC-3	477.62	11.683
16	RPF	483.62	830.989
17	RTC-4	501.61	41.060
18	RTC-5	591.04	4.653
19	RTC-6	607.04	8.913
Total			2742.179

Table 11. The $|\Delta\mathbf{V}|$ Statistics

Type	Entry Interface 3σ Value
Latitude	0.6019 deg
Longitude	0.0229 deg
Flight Path Angle	0.2912 deg
Heading Angle	0.3113 deg

Table 12. The Final Delivery 3σ Statistics with Optical Navigation